UC Berkeley

Title

Probing hydrogen-bond networks in plastic crystals with terahertz and infrared spectroscopy

Permalink

https://escholarship.org/uc/item/5m3349k0

Journal

Cell Reports Physical Science, 3(8)

ISSN

2666-3864

Authors

Lu, Wenchao
Amarasinghe, Chandika
Zhang, Emily
et al.

Publication Date

2022-08-01

DOI

10.1016/j.xcrp.2022.100988

Copyright Information

Peer reviewed

Probing Hydrogen-Bond Networks in Plastic Crystals with Terahertz and Infrared Spectroscopy

Wenchao Lu,[1] Chandika Amarasinghe,[1] Emily Zhang,[1,2] Andrew Martin,[3] Sumanjeet Kaur,[3] Ravi Prasher,[3,4,] and Musahid Ahmed [1,5,]*

[1] Chemical Sciences Division, Lawrence Berkeley National Laboratory, Berkeley, CA 94720, USA

[2] Department of Chemistry, University of California, Berkeley, CA 94720, USA

[3] Energy Storage & Distributed Resources, Lawrence Berkeley National Laboratory, Berkeley, CA 94720, USA

[4] Department of Mechanical Engineering, University of California, Berkeley, CA 94720, USA

[5] Lead Contact

* E-mail: mahmed@lbl.gov

Summary

A molecular-level understanding of phase changes in hydrogen-bonded solid-state systems is of paramount importance in fields spanning thermal science to medical therapeutics. Polyols have recently emerged as prime targets for deployment given their versatility in phase-induced changes and occupy a deep space in eutectic solvents. We explore the hydrogen-bond network of neopentyl glycol (NPG) with terahertz time-domain spectroscopy, attenuated total reflection spectroscopy in the far- and mid-infrared regions augmented by electronic structure calculations. A picture emerges where vibrational spectroscopy can exquisitely probe a crystalline to amorphous solid-solid phase transition while spectroscopy in the mid-infrared region provides a molecular picture of the phase transition. These methods are then applied to understand the thermal properties and phase changes in NPG upon incorporation of bis(trifluoromethane)-sulfonimide lithium salt, to demonstrate that vibrational spectroscopy can directly probe the disruption of hydrogen-bond networks in plastic crystals.

Introduction

Thermal energy accounts for ~50% of global final energy consumption and contributes ~40% of global CO_2 emissions.[1] Thermal energy is roughly split in half for industrial processes and buildings and its decarbonization is one of the biggest grand challenges facing the planet today.[2,3] A fundamental understanding of the underlying processes in materials and molecular systems relevant to thermal energy such as phase transitions, electron-phonon coupling, chemical transformations, condensed phase

thermochemical reactions, and energy conversion is required to tackle these challenges. These processes would have a tremendous economic, societal, and environmental impact, including the realization of long-distance thermal transport, high-energy-density storage, enhanced heat transfer, and improved thermal energy conversion efficiencies.[2] Molecular-scale control of mass and thermal transport at these interfaces is not well understood and falls short of kinetic theory limits by approximately two orders of magnitude for macroscopic systems.

Hydrogen and non-covalent bonding drive myriad processes which have enormous ramifications in molecular growth in soft systems. For instance, subtle changes in pH can drive dramatic changes in protein assembly processes relevant in biology, while a few degrees of change in temperature leads to enormous changes in plastic crystals, systems of much importance in thermal science.[4,5] Phase changes that occur in these multiphasic systems can be tuned by invoking non-covalent interactions that are available in hydrogen-bond liquids,[6] plastic crystals,[7-10] non-crystalline metal-organic frameworks (MOFs),[11-13] and deep eutectic solvents[14]. Polyalcohols provide a motif to develop an understanding of the molecular heterogeneities that occur upon their interaction in aqueous co-solvent systems[15] and application of external energy inputs, particularly temperature.[16] Polyalcohols show significant deviation from ideal behavior upon mixing with solvents, and ions in the bulk environment which is directly a result of micro heterogeneity and liquid-liquid phase separation and solid-solid phase changes, respectively. Indeed recently, dynamic tunability of the transition temperatures of phase change materials based on polyols was demonstrated with the addition of Li-ion salts.[17] This complex behavior provides a rich tapestry to test hydrogen-bond dynamics, probe solvation and confinement and map nucleation and crystallization events.

To probe the effects caused by the change of hydrogen-bond network, we chose neopentyl glycol (NPG), a polyol, as a model system, which has recently garnered much interest for its colossal barocaloric effects and potential application for solid-state refrigeration.[7-9] NPG upon mixing with other polyols has important tunable thermophysical properties which are intimately related to rearrangements of the hydrogen-bond network.[18] However, notwithstanding an enormous body of work[8,9,16,19,20] using simulations, neutron scattering, vibration spectroscopies, differential scanning calorimetry, and X-Ray diffraction, there is still a paucity in understanding the structural and molecular details of the changes in the hydrogen-bond network and the lattice that constitutes NPG. Very recently both the thermal[21] and ionic conductivity[22] in NPG have been studied using atomistic simulations coupled to dielectric spectroscopy. We are motivated by earlier seminal studies that used terahertz (THz) spectroscopy to study solid-state phase transformations[23-29] and THz-driven phase transitions[30-32]. To this end, we will use lab-based THz and infrared (IR) spectroscopy to complement the use of synchrotrons and spallation sources traditionally used

for such studies to probe the physiochemical processes driven by the change of hydrogen-bond network in the solid state. Our approach paves a path for developing tabletop laboratory-based methods for fast characterization which will enable discovery of materials and phenomena leading to rapid development of technologies. We demonstrate this by probing the phase change perturbations on NPG hydrogen-bond network by incorporating a Li-ion salt. A series of studies have probed the hydrogen-bond network of polyols upon addition of salts, particularly bis(trifluoromethane)sulfonimide lithium salt (LiTFSI).[33,34] The interest in LiTFSI originates for preparing Li-ion based room temperature molten salts, crystalline plastics and recently as a dynamic switch for phase change material transition temperatures.[17] We introduced different concentrations of LiTFSI to NPG to probe the changes in the hydrogen-bond network and to elucidate the structural changes in this plastic crystal using our twin probe of terahertz time-domain (THz-TDS) spectroscopy and IR spectroscopy.

Results and Discussion

Probing phase change in NPG with THz and IR spectroscopy

The THz region is sensitive to both the hydrogen-bond network and the lattice structure of molecular crystals, hence application of THz-TDS to NPG, as shown in **Fig. 1A**, reveals the phase changes upon cycling through $30 - 45^{\circ}C$. The heating/cooling rate is roughly $1^{\circ}C/min$, and the temperature is stabilized for at least 10 min per $1^{\circ}C$ increase to minimize hysteresis, in line with previous reports.[8] Our setup measured the phase transition temperature as $41^{\circ}C$ when heating and $32^{\circ}C$ when cooling, consistent with reported phase transition temperature at $41 - 42^{\circ}C$.[8,35] The THz absorption coefficient spectra for low-temperature monoclinic phase show two broad peaks centered at 0.63 THz and 1.29 THz. The 0.63 THz peak disappears after the phase transition to the face-centered cubic (FCC) structure as the temperature is cycled between 30-45 $^{\circ}C$. The absorption as a whole also increases from monoclinic to the FCC structure, while the 1.29 THz peak broadens out. This is because the ordered monoclinic system has a well-defined lattice structure which leads to distinct peaks in the absorption spectra whereas the FCC phase is a disordered plastic crystal which lacks a stable lattice structure. The peak changes upon phase transition can be attributed to the lattice structure difference between the two phases as visualized in the two structures shown in **Fig. 1A**, and the absorption increase is due to the change in dynamics because of the additional disorder of the FCC phase which populates the vibrational density of states at the expense of the better defined (narrower FWHM) vibrational features associated with the monoclinic phase.

Typically, inelastic neutron scattering (INS), and Raman spectroscopy have been used to capture the low-energy region where phase changes occur in molecular organic crystals.[8,9,16] Our THz results can be

directly compared to a recent INS study of the barocaloric effects of NPG using INS,[16] where the dynamic structure factor (S, as a function of momentum transfer and energy transfer of neutrons) was measured at different temperatures to capture the phase changes. At 300 K where NPG exists in the ordered monoclinic form, its measurement, shown as the azure line in **Fig. 1B** reveals a strong peak centered at ~1 THz which disappeared (orange line) after the phase transition. The thick black curve shows the difference between the monoclinic and FCC THz spectra measured in this work, reflecting the contribution caused by the phase transition spectrally, with the peak at ~1 THz matching the INS results well.

Far-infrared (FIR) spectroscopy provides more details of vibrational motions within the crystal lattice. **Fig. 1C** shows FIR spectra of NPG before and after the monoclinic-FCC phase transition using a chip-based attenuated total reflectance Fourier-transform infrared (ATR-FTIR) spectrometer between the region of 150 to 680 cm^{-1}. Sharp peaks are observed for the monoclinic phase (blue line) which disappear or smear out as the phase change occurs (red line). The most dramatic changes are for peaks located at 295, 365, and 524 cm^{-1}. The nature of ATR measurements may bring distortions to the spectrum. We compared the FIR measurements using both ATR and transmission cells and found no major peak shifting (**Fig. S1** of Supplemental Information, SI). The IR spectra of the most stable geometry of NPG tetramer (as a simplified fragment of NPG crystal) are calculated at the ωB97XD/6-31g(d,p) level of theory, to identify the spectroscopic details and to provide a picture of the vibrational modes which are active during the phase transition. The calculated spectrum for the tetramer is highly consistent compared to the experimental spectrum, with all featured absorption bands visible and marked in gray sticks in **Fig. 1C** and the associated modes in **Fig. S2** of SI. These modes in the FIR region are all associated with softening of the lattice leading to more flexibility and low amplitude motions and will disappear or reduce in intensity upon transitioning to the FCC phase.
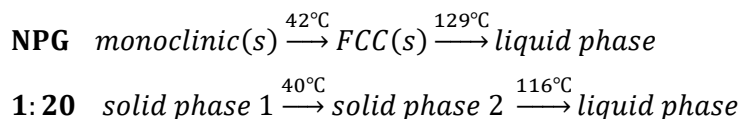
The peaks in the mid-infrared (MIR) region (**Fig. 1D**) can be assigned to particular molecular vibrations. We clearly observe the C-H and O-H bending at 1390 − 1480 cm^{-1} and C-H stretching at 2870 − 2960 cm^{-1}. C-C backbone stretching bands are weak and lie within 1100 − 1300 cm^{-1}. Strong C-O stretching band for the primary alcohol is observed at 1040 cm^{-1}, and a broad O-H stretching is observed around 3300 cm^{-1}. While there are intensity changes in most of the peaks after the phase transition, the most dramatic effect is in the O-H stretching band which blueshifts from 3290 to 3340 cm^{-1}. The FCC lattice has more flexibility compared to the monoclinic crystal lattice, and thus the peak clusters noticed above become smooth, rendering spikes to merge into a broader band. Such flexibility also attenuates the hydrogen-bond network formed within NPG molecules, as less strong hydrogen bonds lead to blueshifts. Our theoretical calculations confirm the assignments associated with each particular mode which can be visualized in the

structures shown in **Fig. S2**. The calculated vibration at 820 cm^{-1} for NPG tetramer, does not appear in the experimental spectrum, since this corresponds to a strong out-of-plane O-H bending which is hindered by the adjacent NPG molecules in an actual crystal lattice but is absent in our calculation.

Phase changes in plastic polyol crystals are usually associated with reorganization of the hydrogen-bond network. The resulted spectral change enables a direct observation of phase transition by tracking featured peaks or frequencies along with the temperature, as shown in **Fig. S3** of SI. As validated by the results above, our spectroscopy-based approach is a promising candidate to provide a rapid and accurate description of the phase transition and depict a detailed molecular-level picture with the reinforcement of theoretical calculations. The THz measurements are comparable to inelastic neutron scattering measurements in THz low-energy regime and are accessible with laboratory-based instruments.

LiTFSI breaks the hydrogen-bond network in NPG

Doping with LiTFSI causes disruption to the hydrogen-bond network, which can affect the thermal and ionic properties of a plastic crystal. We prepared the LiTFSI/NPG mixtures of different molar ratio, with LiTFSI:NPG = 1:20, 1:10, 1:5, 1:2.5, 1:1, 1:0.5, and 1:0.25. For 1:20 and 1:10 samples, the resulting mixture remained waxy solid while higher LiTFSI-containing samples are gel-like liquid, except for 1:0.25 that remains solid again (**Fig. S4** in SI). **Fig. S5** in SI depicts a systematic MIR measurement of each concentration as a function of temperature, with representative spectra shown in **Fig. 2**. It is noteworthy that for the molar ratios of 1:20 and 1:10 (**Fig. 2A – 2D**), we observed an abrupt disappearance of O-H stretching at 3550 cm^{-1}, particularly above 40 $^{\circ}$C, being reminiscent of the phase change in pure NPG. FIR measurements reveal that for molar ratio of 1:20, the spectra at 25 and 50 $^{\circ}$C (before and after the phase transition, respectively) are similar to the phase transition of pure NPG from monoclinic to FCC, while the change of spectral profile for 1:10 is less noticeable. We conducted DSC measurements (**Fig. 3**) for all LiTFSI/NPG concentrations. The DSC curves for LiTFSI/NPG = 1:20 and 1:10 reveal a bulge at 39.5 $^{\circ}$C, which is analogous to a phase transition. After this, the molar ratio of 1:20 equates to a solid-to-solid phase transition similar to that of pure NPG and begins to melt at 116 $^{\circ}$C, whereas the 1:10 mixture begins to melt slowly starting from 40 $^{\circ}$C. Another solid sample, LiTFSI/NPG = 1:0.25, remains solid and its DSC curve is flat within 10 – 130°C. We also performed DSC measurements cycling through 50 – -50 $^{\circ}$C (**Fig. 3b**) for liquid samples. The DSC curves remain flat in this temperature range, indicating no phase change occurred.

$$\textbf{NPG} \quad monoclinic(s) \xrightarrow{42^{\circ}C} FCC(s) \xrightarrow{129^{\circ}C} liquid\ phase$$

$$\textbf{1:20} \quad solid\ phase\ 1 \xrightarrow{40^{\circ}C} solid\ phase\ 2 \xrightarrow{116^{\circ}C} liquid\ phase$$

$$1:10 \quad solid\ phase \xrightarrow{40℃} slowly\ transition\ to\ liquid\ phase$$

Fig. 2E and 2F are a snapshot of how the LiTFSI changes the overall hydrogen-bond network of NPG crystal lattice. In the FIR regime, the spectral profiles gradually increase absorption as a function of LiTFSI %, with isosbestic points at 526 and 546 cm^{-1}. In comparison with pure NPG, the MIR spectra of the mixtures shown in Fig. 2B, 2D and 2F, we see several bands from 1000 – 1400 cm^{-1} which are the vibrational bands of the TFSI anion backbone (asymmetric S–N–S stretching at 1062 cm^{-1}; C–SO$_2$–N bonding mode at 1143 cm^{-1}; asymmetric stretching mode of C-F at 1193 cm^{-1}; asymmetric O=S=O stretching mode at 1357 cm^{-1}).[36] The most intriguing peak is the hydroxyl of NPG at 3200 – 3700 cm^{-1}. A second sharp O-H stretching peak emerges at around 3550 cm^{-1} (Fig. 2F), and this peak becomes dominant over the H-bonded broad O-H band as the LiTFSI concentration increases. As the molar ratio of LiTFSI/NPG continues to increase to 1:0.5, only the second O-H remains in the spectrum. Tran et al. have also noticed a similar second O-H stretching as the concentration of LiTFSI increases in LiTFSI/ethylene glycol system.[33] This peak is attributed to O-H stretching free from intermolecular H bonds but with intramolecular H bonds, as a previous study showed that O-H stretching of an alcohol diluted in a non-polar solvent like CCl$_4$, free from hydrogen bonds, is around 3630 cm^{-1} while an intramolecular hydrogen-bonded O-H stretching shows an absorption peak around 3590 cm^{-1}.[37] Since TFSI anion is the conjugate base of the superacid, HTFSI, it exhibits less nucleophilicity due to the charge dispersion induced by strong electron-withdrawing groups. The addition of the large TFSI anion destroys the crystal lattice, leaving free NPG monomers to form intramolecular H bonds between the two hydroxyls.

We have plotted the absorption of 4 featured bands vs. the molar ratio of LiTFSI/NPG: 1200 cm^{-1} (C-F stretching, LiTFSI exclusive), 2960 cm^{-1} (C-H stretching, NPG exclusive), ~3350 cm^{-1} for intermolecular H-bonded O-H stretching and ~3550 cm^{-1} for intramolecular H-bonded O-H stretching (Fig. 4 and Fig. S6 in SI). The intensity of absorption band at 1200 and 2960 cm^{-1} correlates to the concentration of LiFTSI and NPG. The O-H stretching peak is fitted using Gaussian functions showing the contribution of two types of O-H vibrational modes, as shown in Fig. S7 in the SI. Note that for LiTFSI:NPG = 1:0.5 and 1:0.25, the Gaussian fitting for the O-H stretching at ~3350 cm^{-1} is negligible, and a direct reading of the absorption at 3350 cm^{-1} is adopted as the contribution of H-bonded O-H. We plot the wavenumber and absorption changes of two O-H stretching modes vs. temperature, as shown in Fig. S8 in SI. The addition of LiTFSI weakens the intensity of intermolecular H-bonded O-H stretching as a blueshift is noted for higher concentrations of LiTFSI (Fig. S8A in SI), indicating a gradual dilution of NPG together with the attenuation of the surrounding hydrogen bonds. The absorption trends of H-bonded O-H stretching together with the

corresponding Van't Hoff plot are shown in **Fig. S8B** and **S8C** in SI. By comparing with the profile of pure NPG, a phase transition at ~40°C is observed for LiTFSI:NPG = 1:20 and 1:10, whereas the changes for higher LiTFSI concentrations are negligible. The absorption of the intermolecular H-bonded O-H stretching at ~3550 cm^{-1} reaches the maximum at LiTFSI/NPG = 1:2.5 to 1:1 and decreases at higher LiTFSI concentrations. This is due to the synergistic effect between the increasing percentage of intramolecular vs. intermolecular H-bonded O-H stretching and the concentration decrease of NPG, as the only source of -OH. Even at 1:1 concentration, TFSI anion almost completely attenuated the hydrogen-bond network formed within NPG molecules, which is rather efficient. In short, our investigation of doping LiTFSI into NPG shows very apparent and efficient suppression for the hydrogen-bond network. It is worth noting that for intermolecular H-bonded O-H stretching, a turning point is observed at the molar ratio of LiTFSI/NPG = 1:2.5. This suggests a concentration with the highest efficacy of LiTFSI participating in reorganizing the hydrogen-bond network.

The molecular visualization of disorder that emerges into crystalline materials described here is readily applicable for probing phase transitions in thermal systems and can also be extended to probe ion transport in plastic crystals and nucleation and crystallization of materials of relevance to energy science and pharma.[38,39] THz spectroscopy has recently been applied to probe microscopic ion migration in solid electrolytes upon temperature cycling,[40] while there is enormous interest in understanding ion diffusion, particularly Li in deep eutectic solvents with vibrational spectroscopy.[34,41] Our methods will find ready applications here. The THz spectra (**Fig. S9**) show a similar phase-transition scenario for LiTFSI/NPG = 1:20 and 1:10 mixtures. The spectrum recorded at 50°C, which is after the phase transition, shows blueshifts to each major peak, and the overall profile is smoother, indicating a relaxed crystal lattice. The high-temperature measurements for 1:20 and 1:10 are very similar, with 1:20 peaks at slightly higher frequencies compared to 1:10. Our methods can be applied to other salts and organic moieties where a predictive capability for thermal and transport properties can be discerned by a quick visualization of the vibrational spectroscopy as a function of mixture concentrations.

Conclusion

We have demonstrated the application of THz time-domain spectroscopy and chip-based attenuated total reflection spectroscopy to probe phase changes in a plastic crystal, NPG and the effect on its hydrogen-bond network upon introducing a salt, LiTFSI. A breakdown in the hydrogen-bond network in NPG upon temperature cycling from the monoclinic to FCC structure is revealed in the spectroscopy. A gas-phase

density functional calculation on the NPG tetramer can capture the essential structure of the monoclinic phase in NPG. The molecular details of this phase change along with disruption of the hydrogen-bond network by LiTFSI can be followed by a chip-based ATR-FTIR spectrometer. Our spectroscopy-based approach promises to provide a rapid, accurate and inexpensive approach to capture disruptions of the hydrogen-bond network at a molecular level, which is ubiquitous in phase-change processes within plastic crystals and deep eutectic solvents.

Experimental Procedures

Resource availability

Lead contact

Further information and requests for the resources are available from the lead contact, Musahid Ahmed (mahmed@lbl.gov).

Materials availability

The materials described in this study can be made available upon request.

Data and code availability

All data reported in this article are available from the lead contact upon reasonable request.

Chemicals and Sample Preparation

Bis(trifluoromethane)sulfonimide lithium salt (LiTFSI, 99.95%) and 2,2-dimethyl-1,3-propanediol, also known as neopentyl glycol (NPG, 99%) were purchased from Sigma-Aldrich and used without further purification. The mixtures of LiTFSI/NPG were prepared at molar ratios of 1:20, 1:10, 1:5, 1:2.5, 1:1, 1:0.5, and 1:0.25. As LiTFSI is very hygroscopic, the two chemicals were weighed and mixed with nitrogen constantly purging the space. Successively, an equal volume of ethanol was added to completely dissolve the mixture. The clear ethanol solutions of LiTFSI/NPG were placed in a furnace (MTI Corporation, KSL-1200X) heated up to 150 $^{\circ}$C for 1 hour to fully expel ethanol and water in the mixture. The IR spectra of samples show no featured absorption at 428 cm^{-1} (from ethanol) and negligible H-O-H scissoring at 1634 cm^{-1} (from water).

Terahertz Time-Domain Spectroscopy

The THz spectra were acquired using a commercial THz system (Tera K15, Menlo Systems). It consists of a 1560 nm fiber-coupled femtosecond laser where the output is split into two, one pumps the THz emitter and the other goes to the optomechanical delay line. The emitted THz light is focused on our sample with a focused area of 3 mm (H) × 10 mm (w). During the measurements, dry nitrogen gas was constantly purged into the system to reduce the effects from air and water vapor. We used a Specac omni cell with a 3D printed holder to mount the cell and to ensure that we placed the cell at the same position for all our experiments. The samples were placed between two polythene windows of 3 mm thickness with a 1 mm spacer between them. The experimental configuration is visualized in **Fig. S10** in SI. For LiTFSI/NPG mixtures, the sample was first heated to melt and then poured into a quartz cuvette for the measurements, with all other configurations kept the same. The collection time for each measurement was set to 100 s in reference to an empty sample cell, and each measurement is an average of 2000 scans. The dynamic range is ~ 0.3 – 2.5 THz. The sample was heated using a round ceramic heater which had an inner diameter of 4 mm and outer diameter of 23 mm. Therefore, the effective sample probe area is limited to the opening of the heater. The resulting

time pulse from the sample was detected from the THz detector. The detector is only sensitive if both pump and THz pulses arrive simultaneously. Thus, by scanning the ODL, we measure the THz field as a function of time. This gives information of both amplitude and the phase of the field from which we can calculate both the refractive index and the absorption of the material in the THz region. THz spectra were analyzed using TeraMAT and TeraLyzer software (Menlo Systems). Reasonable truncation was applied to the time-domain waveform to remove Fabry–Perot reflections and thus reduce the high-frequency noise. It is worth mentioning that the sharp features of the measurements of LiTFSI:NPG = 1:20 and 1:10 (**Fig. S9**) are artifacts caused by possible beam divergence and clipping due to the limitation of our heating cell configuration and cannot be eliminated by repeating the test with the same reference geometry.

Fourier-Transform Infrared-Attenuated Total Reflection (FTIR-ATR) Spectroscopy

The FTIR spectra were collected using a Bruker VERTEX 70 FTIR spectrometer coupled with a silicon-based ATR device (IRUBIS) for both mid-infrared (MIR) and far-infrared (FIR) measurements. The parameters of ATR setup are optimized by the manufacturer, with a single-bounce reflection and 26.7° for the inner angle of incidence (20° for the outer angle of incidence). A customized copper sample holder is directly mounted on top of the ATR chip, sealed by a 9 mm O.D. × 7 mm I.D. O-ring that allows for a constant contact area between the ATR chip and LiFTSI/NPG samples. A ceramic heater with temperature control (Thorlabs TC200) was connected to the sample holder to precisely monitor and tune the temperature of the samples. The experimental configuration is visualized in **Fig. S11** in SI. Each measurement was performed only after the temperature became stable. The spectral scan range was set to 600 – 4000 cm^{-1} for MIR and 150 - 680 cm^{-1} for FIR measurements. Each measurement is averaged by 16 scans, and the spectral resolution is set to 4 cm^{-1}. The spectrometer is constantly purged using dry nitrogen gas during FIR measurements.

In the ATR configuration, the spectrum varies from a conventional transmission spectrum because the light penetrates the material at a depth proportionate to the wavelength. As a result, the absorbances in an ATR-measured spectrum are proportionally greater at lower frequencies than at higher frequencies, causing distortion to both the peak frequencies and band intensities.[42] Correction algorithm is available to convert an ATR spectrum to a conventional transmission/absorption spectrum.[43] In our measurements, the obtained MIR-ATR spectra were corrected using the advanced ATR correction function available in the OMNIC software package (Thermo Scientific) with refractive indices of NPG 1.44, LiTFSI 1.38, and the mixtures ~ 1.40.

Differential Scanning Calorimetry (DSC) Analysis:

DSC (Model DSC2500, TA Instruments) was employed to investigate the phase transition behavior of LiTFSI/NPG samples. The sample was sealed with a hermetically sealed aluminum lid. The sample is equilibrated at 20°C and then heated from 20 to 110°C for LiTFSI/NPG = 1:20, 1:10 and 1:0.25 (solids) and lowered from 50 to -50°C for LiTFSI/NPG

= 1:5, 1:2.5, 1:1 and 1:0.5 (liquids) with a heating/cooling rate of 1°C/min. Data analysis was done using TA TRIOS software.

Theoretical Calculations

To compare with experimental results, the IR spectrum for gas-phase NPG tetramer was calculated at ωB97XD/6-31g(d,p) using Gaussian 09.[44] The calculated vibrational frequencies are scaled by 0.943.[45] The convergence criteria are the default settings in Gaussian 09, i.e., maximum force change is below 0.000450 Hartrees/Bohr and maximum displacement change below 0.001800 Hartrees/Radians. Our DFT calculation only serves as a molecular visualization of each IR band, which is more related to specific bond motion rather than the influence from the crystal lattice. The optimized geometry of the NPG tetramer is available as **Note S1** in the SI.

Supplemental Information

Supplemental information can be found online at:

Author Contributions:

M.A., R.P. and S.K. conceived the idea to probe the hydrogen-bond network in plastic crystals with salts for thermal energy science. W.L. performed the FTIR measurements, data analysis and theoretical calculations, C.A. and E.Z. performed the THz-TDS measurements, and A.M. performed the DSC measurements. M.A. and W.L. wrote the manuscript with active participation from R.P., S.K. and C.A. All authors discussed the data and interpretation of results. M.A. supervised the project.

Declaration of Interests

The authors declare no conflict of interest.

References:

1. IEA (2019). Renewables 2019. IEA. https://www.iea.org/reports/renewables-2019.
2. Henry, A., Prasher, R., and Majumdar, A. (2020). Five thermal energy grand challenges for decarbonization. Nat. Energy *5*, 635-637. https://doi.org/10.1038/s41560-020-0675-9.
3. The heat is on. (2016). Nat. Energy *1*, 16193. https://doi.org/10.1038/nenergy.2016.193.
4. Matuszek, K., Vijayaraghavan, R., Kar, M., and MacFarlane, D.R. (2020). Role of hydrogen bonding in phase change materials. Cryst. Growth Des. *20*, 1285-1291. https://doi.org/10.1021/acs.cgd.9b01541.
5. Moya, X., and Mathur, N.D. (2020). Caloric materials for cooling and heating. Science *370*, 797-803. https://doi.org/10.1126/science.abb0973.
6. Shao, X.-F., Wang, C., Yang, Y.-J., Feng, B., Zhu, Z.-Q., Wang, W.-J., Zeng, Y., and Fan, L.-W. (2018). Screening of sugar alcohols and their binary eutectic mixtures as phase change materials for low-to-medium temperature latent heat storage. (Ⅰ): Non-isothermal melting and crystallization behaviors. Energy *160*, 1078-1090. https://doi.org/10.1016/j.energy.2018.07.081.
7. Rosenberg, D.J., Alayoglu, S., Kostecki, R., and Ahmed, M. (2019). Synthesis of microporous silica nanoparticles to study water phase transitions by vibrational spectroscopy. Nanoscale Adv. *1*, 4878-4887. https://doi.org/10.1039/C9NA00544G.
8. Lloveras, P., Aznar, A., Barrio, M., Negrier, P., Popescu, C., Planes, A., Mañosa, L., Stern-Taulats, E., Avramenko, A., Mathur, N.D., et al. (2019). Colossal barocaloric effects near room temperature in plastic crystals of neopentylglycol. Nat. Commun. *10*, 1803. https://doi.org/10.1038/s41467-019-09730-9.
9. Li, F.B., Li, M., Xu, X., Yang, Z.C., Xu, H., Jia, C.K., Li, K., He, J., Li, B., and Wang, H. (2020). Understanding colossal barocaloric effects in plastic crystals. Nat. Commun. *11*, 4190. https://doi.org/10.1038/s41467-020-18043-1.
10. Mañosa, L., and Planes, A. (2020). Solid-state cooling by stress: A perspective. Appl. Phys. Lett. *116*, 050501. https://doi.org/10.1063/1.5140555.
11. McGillicuddy, R.D., Thapa, S., Wenny, M.B., Gonzalez, M.I., and Mason, J.A. (2020). Metal–organic phase-change materials for thermal energy storage. J. Am. Chem. Soc. *142*, 19170-19180. https://doi.org/10.1021/jacs.0c08777.
12. Pattengale, B., Neu, J., Ostresh, S., Hu, G., Spies, J.A., Okabe, R., Brudvig, G.W., and Schmuttenmaer, C.A. (2019). Metal–organic framework photoconductivity via time-resolved terahertz spectroscopy. J. Am. Chem. Soc. *141*, 9793-9797. https://doi.org/10.1021/jacs.9b04338.
13. Ennis, C., Tay, A.C.Y., Falconer, J.L., Lee, S.J., and Meledandri, C.J. (2021). Nanoscale Cu(II) MOFs formed via microemulsion: vibrational mode characterization performed using a combined FTIR, synchrotron far-IR, and periodic DFT approach. J. Phys. Chem. C *125*, 20426-20438. https://doi.org/10.1021/acs.jpcc.1c06227.
14. Kaur, S., Kumari, M., and Kashyap, H.K. (2020). Microstructure of deep eutectic solvents: Current understanding and challenges. J. Phys. Chem. B *124*, 10601-10616. https://doi.org/10.1021/acs.jpcb.0c07934.
15. Oh, K.-I., and Baiz, C.R. (2020). Molecular heterogeneity in aqueous cosolvent systems. J. Chem. Phys. *152*, 190901. https://doi.org/10.1063/5.0007647.
16. Li, B., Kawakita, Y., Ohira-Kawamura, S., Sugahara, T., Wang, H., Wang, J., Chen, Y., Kawaguchi, S.I., Kawaguchi, S., Ohara, K., et al. (2019). Colossal barocaloric effects in plastic crystals. Nature *567*, 506-510. https://doi.org/10.1038/s41586-019-1042-5.
17. Lau, J., Papp, J.K., Lilley, D., Khomein, P., Kaur, S., Dames, C., Liu, G., and Prasher, R. (2021). Dynamic tunability of phase-change material transition temperatures using ions for thermal

energy storage. Cell Reports Physical Science *2*, 100613. https://doi.org/10.1016/j.xcrp.2021.100613.

18. Chandra, D., Day, C.S., and Barrett, C.S. (2013). Low- and high-temperature structures of neopentylglycol plastic crystal. Powder Diffr. *8*, 109-117. https://doi.org/10.1017/S0885715600017930.

19. Benson, D.K., Burrows, R.W., and Webb, J.D. (1986). Solid state phase transitions in pentaerythritol and related polyhydric alcohols. Solar Energy Materials *13*, 133-152. https://doi.org/10.1016/0165-1633(86)90040-7.

20. Feng, H., Liu, X., He, S., Wu, K., and Zhang, J. (2000). Studies on solid–solid phase transitions of polyols by infrared spectroscopy. Thermochim. Acta *348*, 175-179. https://doi.org/10.1016/S0040-6031(99)00403-7.

21. Wang, S., Sun, L., Li, B., and Dai, L. (2021). Atomistic insights into the anisotropic and low thermal conductivity in neopentyl glycol crystals: A molecular dynamics study. J. Phys. Chem. C *125*, 15853-15862. https://doi.org/10.1021/acs.jpcc.1c04035.

22. Pan, H., Luo, J., Li, B., and Wübbenhorst, M. (2021). Phase-dependent dielectric properties and proton conduction of neopentyl glycol. RSC Adv. *11*, 23228-23234. https://doi.org/10.1039/D1RA03366B.

23. Jepsen, P.U., Fischer, B.M., Thoman, A., Helm, H., Suh, J.Y., Lopez, R., and Haglund, R.F. (2006). Metal-insulator phase transition in a VO_2 thin film observed with terahertz spectroscopy. Phys. Rev. B *74*, 205103. https://doi.org/10.1103/PhysRevB.74.205103.

24. Delaney, S.P., Smith, T.M., Pan, D., Yin, S.X., and Korter, T.M. (2014). Low-temperature phase transition in crystalline aripiprazole leads to an eighth polymorph. Cryst. Growth Des. *14*, 5004-5010. https://doi.org/10.1021/cg500569x.

25. Nickel, D.V., Delaney, S.P., Bian, H., Zheng, J., Korter, T.M., and Mittleman, D.M. (2014). Terahertz vibrational modes of the rigid crystal phase of succinonitrile. J. Phys. Chem. A *118*, 2442-2446. https://doi.org/10.1021/jp411865n.

26. Ruggiero, M.T., Zeitler, J.A., and Erba, A. (2017). Intermolecular anharmonicity in molecular crystals: interplay between experimental low-frequency dynamics and quantum quasi-harmonic simulations of solid purine. Chem. Commun. *53*, 3781-3784. https://doi.org/10.1039/C7CC00509A.

27. Ruggiero, M.T., Kölbel, J., Li, Q., and Zeitler, J.A. (2018). Predicting the structures and associated phase transition mechanisms in disordered crystals via a combination of experimental and theoretical methods. Faraday Discuss. *211*, 425-439. https://doi.org/10.1039/C8FD00042E.

28. Ruggiero, M.T., Zhang, W., Bond, A.D., Mittleman, D.M., and Zeitler, J.A. (2018). Uncovering the connection between low-frequency dynamics and phase transformation phenomena in molecular solids. Phys. Rev. Lett. *120*, 196002. https://doi.org/10.1103/PhysRevLett.120.196002.

29. Kölbel, J., Li, Q., Threlfall, T.L., and Zeitler, J.A. (2022). Measuring solute concentration with terahertz time-domain spectroscopy in single and multiphase systems. Anal. Chem. *94*, 1713-1716. https://doi.org/10.1021/acs.analchem.1c04279.

30. Zalden, P., Shu, M.J., Chen, F., Wu, X., Zhu, Y., Wen, H., Johnston, S., Shen, Z.-X., Landreman, P., Brongersma, M., et al. (2016). Picosecond electric-field-induced threshold switching in phase-change materials. Phys. Rev. Lett. *117*, 067601. https://doi.org/10.1103/PhysRevLett.117.067601.

31. Wade, C.G., Marcuzzi, M., Levi, E., Kondo, J.M., Lesanovsky, I., Adams, C.S., and Weatherill, K.J. (2018). A terahertz-driven non-equilibrium phase transition in a room temperature atomic vapour. Nat. Commun. *9*, 3567. https://doi.org/10.1038/s41467-018-05597-4.

32. Zhou, J., and Zhang, S. (2021). Terahertz optics-driven phase transition in two-dimensional multiferroics. npj 2D Mater. Appl. *5*, 16. https://doi.org/10.1038/s41699-020-00189-7.

33. Tran, K.T.T., Le, L.T.M., Phan, A.L.B., Tran, P.H., Vo, T.D., Truong, T.T.T., Nguyen, N.T.B., Garg, A., Le, P.M.L., and Tran, M.V. (2020). New deep eutectic solvents based on ethylene glycol - LiTFSI and their application as an electrolyte in electrochemical double layer capacitor (EDLC). J. Mol. Liq. *320*, 114495. https://doi.org/10.1016/j.molliq.2020.114495.

34. Dinh, T.T.A., Huynh, T.T.K., Le, L.T.M., Truong, T.T.T., Nguyen, O.H., Tran, K.T.T., Tran, M.V., Tran, P.H., Kaveevivitchai, W., and Le, P.M.L. (2020). Deep eutectic solvent based on lithium bis[(trifluoromethyl)sulfonyl] imide (LiTFSI) and 2,2,2-trifluoroacetamide (TFA) as a promising electrolyte for a high voltage lithium-ion battery with a $LiMn_2O_4$ cathode. ACS Omega *5*, 23843-23853. https://doi.org/10.1021/acsomega.0c03099.

35. Sarı, A., Alkan, C., and Bicer, A. (2013). Development, characterization, and latent heat thermal energy storage properties of neopentyl glycol-fatty acid esters as new solid–liquid PCMs. Ind. Eng. Chem. Res. *52*, 18269-18275. https://doi.org/10.1021/ie403039n.

36. Kam, W., Liew, C.-W., Lim, J.Y., and Ramesh, S. (2014). Electrical, structural, and thermal studies of antimony trioxide-doped poly(acrylic acid)-based composite polymer electrolytes. Ionics *20*, 665-674. https://doi.org/10.1007/s11581-013-1012-0.

37. Ma, X., and Wang, J. (2009). Differentiating subtle variation of weak intramolecular hydrogen bond in vicinal diols by linear infrared spectroscopy. J. Phys. Chem. A *113*, 6070-6076. https://doi.org/10.1021/jp9016085.

38. Bryant, S.J., Christofferson, A.J., Greaves, T.L., McConville, C.F., Bryant, G., and Elbourne, A. (2022). Bulk and interfacial nanostructure and properties in deep eutectic solvents: Current perspectives and future directions. J. Colloid Interface Sci. *608*, 2430-2454. https://doi.org/10.1016/j.jcis.2021.10.163.

39. Sibik, J., and Zeitler, J.A. (2016). Direct measurement of molecular mobility and crystallisation of amorphous pharmaceuticals using terahertz spectroscopy. Adv. Drug Deliv. Rev. *100*, 147-157. https://doi.org/10.1016/j.addr.2015.12.021.

40. Morimoto, T., Nagai, M., Minowa, Y., Ashida, M., Yokotani, Y., Okuyama, Y., and Kani, Y. (2019). Microscopic ion migration in solid electrolytes revealed by terahertz time-domain spectroscopy. Nat. Commun. *10*, 2662. https://doi.org/10.1038/s41467-019-10501-9.

41. Jaumaux, P., Liu, Q., Zhou, D., Xu, X., Wang, T., Wang, Y., Kang, F., Li, B., and Wang, G. (2020). Deep-eutectic-solvent-based self-healing polymer electrolyte for safe and long-Life lithium-metal batteries. Angew. Chem. Int. Ed. *59*, 9134-9142. https://doi.org/10.1002/anie.202001793.

42. Larkin, P.J. (2018). Instrumentation and Sampling Methods, Chapter 3. In Infrared and Raman Spectroscopy (Second Edition), P.J. Larkin, ed. (Elsevier), pp. 29-61. https://doi.org/10.1016/B978-0-12-804162-8.00003-3.

43. Nunn, S., and Nishikida, K. (2008). Advanced ATR correction algorithm, Application Note: 50581, Thermo Fisher Scientific, Madison, WI, USA.

44. Frisch, M.J., Trucks, G.W., Schlegel, H.B., Scuseria, G.E., Robb, M.A., Cheeseman, J.R., Scalmani, G., Barone, V., Mennucci, B., Petersson, G.A., et al. (2010). Gaussian 09, Revision C.01 (Gaussian, Inc., Wallingford CT).

45. Alecu, I.M., Zheng, J., Zhao, Y., and Truhlar, D.G. (2010). Computational thermochemistry: Scale factor databases and scale factors for vibrational frequencies obtained from electronic model chemistries. J. Chem. Theory Comput. *6*, 2872-2887. https://doi.org/10.1021/ct100326h.
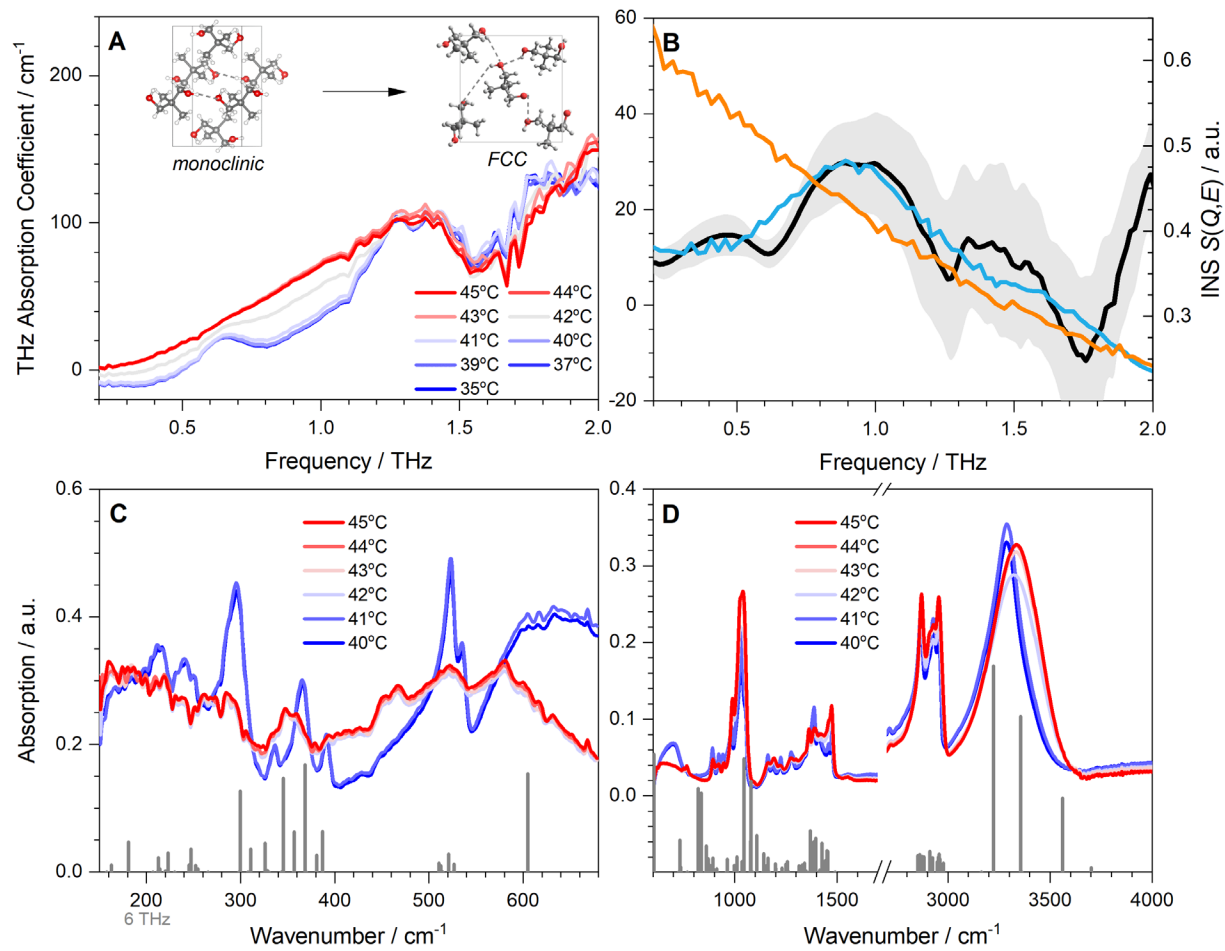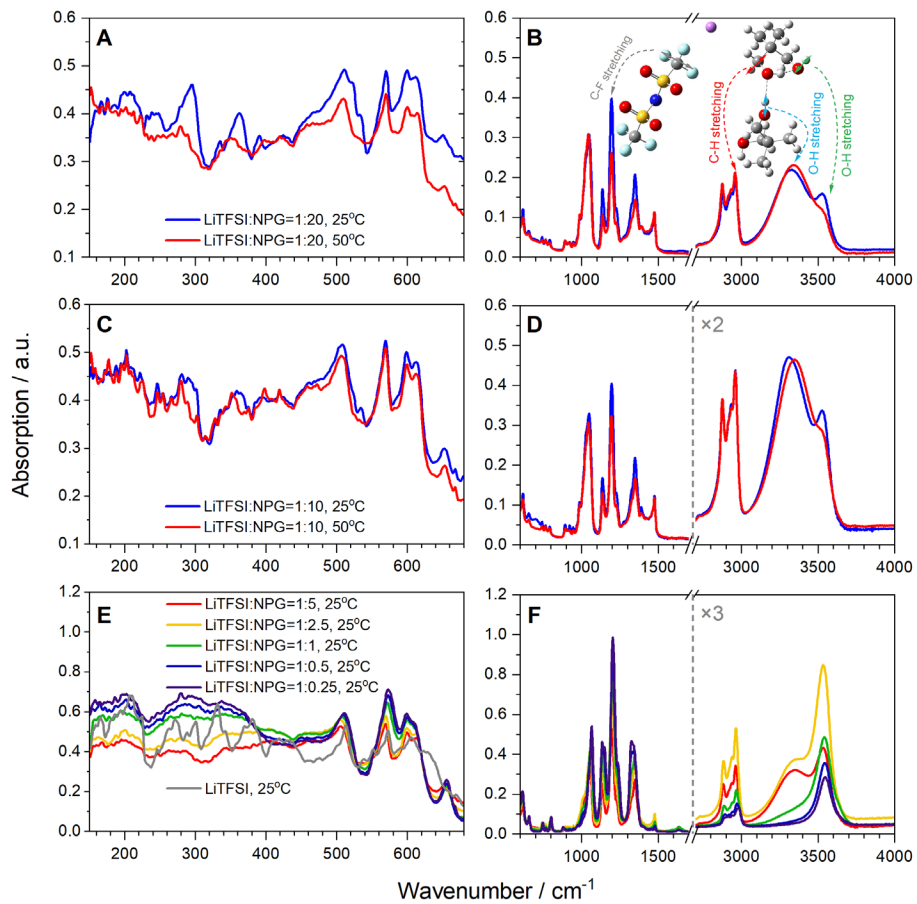
Figure Captions

Figure 1   Spectroscopies of monoclinic and FCC NPG. (A) THz-TDS of monoclinic (blue) and FCC (red) NPG; (B) THz absorption difference between monoclinic and FCC NPG in comparison to dynamic structure factor of monoclinic (azure curve) and FCC (orange curve) NPG from inelastic neutron scattering (from Ref. 16). (C) ATR-FIR, and (D) ATR-MIR spectra of monoclinic (blue) and FCC (red) NPG, in comparison to the DFT-calculated IR frequencies of NPG tetramer (gray vertical lines in each frame) along with the x-axis. ATR-MIR spectra are corrected using advanced ATR correction algorithm. The x-axis break from $1700 - 2700$ cm^{-1} in (D) does not contain any apparent peaks.
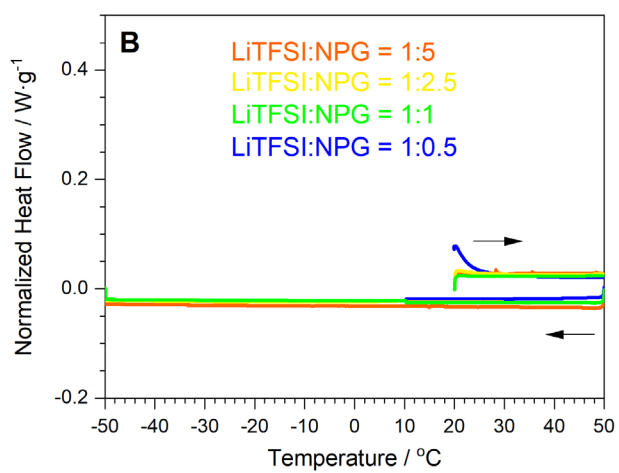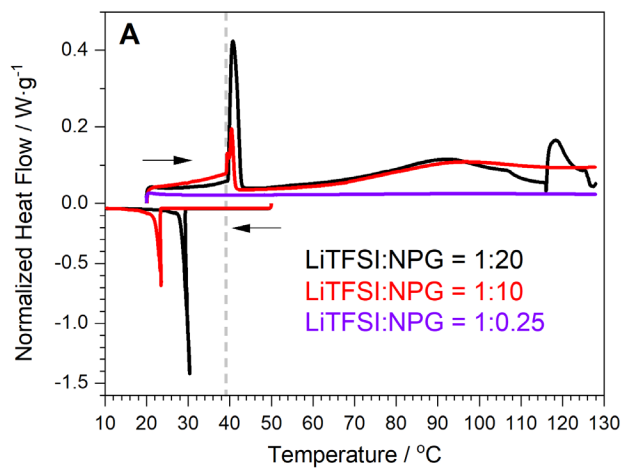
Figure 2   ATR-FIR and ATR-MIR spectra of LiTFSI/NPG mixtures. (A $-$ D) Spectra of LiTFSI:NPG = 1:20 and 1:10 by moles, collected at 25 $^{\circ}$C (blue) and 50 $^{\circ}$C (red). A pseudo phase transition similar to pure NPG is observed at ~40°C. (E $-$ F) Spectra of LiTFSI:NPG = 1:5, 1:2.5, 1:1, 1:0.5, and 1:0.25. All ATR-MIR spectra are corrected using advanced ATR correction algorithm. The x-axis break from $1700 - 2700$ cm^{-1} in (B), (D), and (F) does not contain any apparent peaks.

Figure 3   DSC curves of all concentrations of LiTFSI/NPG mixtures. (A) DSC curves for NPG:LiTFSI = 1:20, 1:10 and 1:0.25 solids cycled through $20 - 130$ $^{\circ}$C. A phase transition at the temperature of 39.5°C for 1:20 and 1:10 is observed; and (B) DSC curves for NPG:LiTFSI = 1:5, 1:2.5; 1:1 and 1:0.5 liquids cycled through $20 - 50$ $^{\circ}$C and $50 - -50$ $^{\circ}$C. The black arrows indicate the direction of the endotherm/exotherm.

Figure 4   MIR absorption change as a function of molar percentage of LiTFSI. Four peak positions indicating the signature band of: (A) C-F stretching of TFSI anion at 1200 cm^{-1}, (B) C-H stretching of NPG at 2960 cm^{-1}, (C) intermolecular O-H stretching at 3350 cm^{-1} and (D) the new intramolecular O-H stretching at 3550 cm^{-1}, vs. the molar percentage of LiTFSI in the mixture at temperatures of 25 $^{\circ}$C, 40°C, 50°C, 60°C, and 70 $^{\circ}$C. The turning point at (D) indicates the highest efficacy of LiTFSI participating in reorganization of the hydrogen-bond network. The absorptions of two types of O-H stretching modes are obtained by a two-peak Gaussian fitting centered at 3350 cm^{-1} and 3550 cm^{-1}.

LiTFSI / NPG Ratio vs. Absorption